ELSEVIER

Nuclear Physics A 676 (2000) 371–387

NUCLEAR PHYSICS A

www.elsevier.nl/locate/npe

Σ^-p elastic-scattering in the region of $400 < p_{\Sigma^-} < 700$ MeV/c with a scintillating-fiber active target

KEK-PS E289 collaboration

Y. Kondo [a], J.K. Ahn [a,1], H. Akikawa [a], J. Arvieux [b,2], B. Bassalleck [c], M.S. Chung [d,3], H. En'yo [a], T. Fukuda [e,4], H. Funahashi [a], S.V. Golovkin [f], A.M. Gorin [f], Y. Goto [a,5], M. Hanabata [g], T. Hayakawa [h], A. Ichikawa [a], M. Ieiri [i], K. Imai [a], M. Ishino [a], H. Kanda [a,6], Y.D. Kim [i,7], E.N. Kozarenko [j], I.E. Kreslo [j], J.M. Lee [k,8], A. Masaike [a,9], S. Mihara [a,10], K. Nakai [h], K. Nakazawa [g], K. Ozawa [a], A. Sato [h], H.D. Sato [a], K.S. Sim [d], T. Tabaru [a], F. Takeutchi [l], P. Tlustý [e,11], H. Torii [a], K. Yamamoto [a,12], S. Yokkaichi [a], M. Yoshida [a,5]

[a] *Department of Physics, Kyoto University, Kyoto 606-8502, Japan*
[b] *Laboratory National Saturne, F-91191, Gif-sur-Yvette cedex, France*
[c] *Department of Physics, University of New Mexico, NM 87131, USA*
[d] *Department of Physics, Korea University, Seoul 136-701, Korea*
[e] *Institute for Nuclear Study, University of Tokyo, Tanashi, Tokyo 188-0002, Japan*
[f] *Institute for High Energy Physics, RU-142284, Protvino, Russia*
[g] *Physics Department, Gifu University, Gifu 501-1193, Japan*
[h] *Department of Physics, Science University of Tokyo, Noda, Chiba 278-8510, Japan*
[i] *KEK, High Energy Accelerator Research Organization, Tsukuba 305-0801, Japan*
[j] *Joint Institute for Nuclear Research, RU-141980, Dubna, Russia*
[k] *Department of Physics, Yonsei University, Seoul 120-749, Korea*
[l] *Department of Physics, Kyoto Sangyo University, Kyoto 603-8555, Japan*

Received 1 March 2000; revised 29 March 2000; accepted 3 April 2000

[1] Present address: Reseach Center for Nuclear Physics, Osaka University, Ibaraki, Osaka 567-0047, Japan.
[2] Present address: Institut de Physique Nucléaire, Université Paris-Sud, 91406 Orsay, France.
[3] Present address: Los Alamos National Laboratory, Los Alamos, NM 87545, USA.
[4] Present address: KEK, High Energy Accelerator Research Organization, Tsukuba 305-0801, Japan.
[5] Present address: RIKEN, Institute of Physical and Chemical Research, Wako, Saitama 351-0198, Japan.
[6] Present address: Physics Department, Graduate School of Science, Tohoku University, Sendai 980-8578, Japan.
[7] Present address: Physics Department, Sejong University, Seoul, 143-747, Korea.
[8] Present address: Korea Research Institute of Standards and Science, Taejon, 305-600, Korea.
[9] Present address: Fukui University of Technology, Fukui 910-8505, Japan.
[10] Present address: International Center for Elementary Particle Physics, University of Tokyo, Tokyo 113-0033, Japan.
[11] Present address: Nuclear Physics Institute of the Academy of Science, 250 68 Řež, Czech Republic.
[12] Present address: Deparment of Physics, Osaka City University, Osaka 558-8585, Japan.

0375-9474/00/$ – see front matter
PII: S0375-9474(00)00191-3

Abstract

We have performed a hyperon-proton scattering experiment with a scintillating fiber active target. The Σ^-p, Λp and Σ^+p scattering have been studied with the same experimental setup. In this paper, we present the differential cross sections of the Σ^-p elastic scattering in the momentum region from 400 to 700 MeV/c. This is the first measurement of the Σ^-p elastic scattering in the momentum region where the P- and higher waves contributions are important. The present data are in good agreement with the one boson exchange model (Bonn–Jülich model A) and the quark cluster model (FSS of Kyoto–Niigata model).

PACS: 13.75.Ev; 21.30.Cb; 25.60.Bx; 25.80.Pw

Keywords: Σ^-p elastic scattering; Hyperon–nucleon interaction; Differential cross sections; Scintillating fiber active target

1. Introduction

The strong interaction in the perturbative region is well described by quantum chromodynamics (QCD). However, it is still a quite difficult problem to derive the nuclear interaction from QCD. Although the nucleon–nucleon (NN) interaction has been well described by the meson exchange picture, there are various methods to treat the short-range repulsive forces. It is believed that effects from the quark–gluon structure of nucleons should appear in the short-range forces. In order to understand the strong interaction in the nonperturbative region, studies of interactions between various baryons play a very important role. The one boson exchange (OBE) models have been developed with the abundant experimental data of the NN scattering, and have been extended to describe the hyperon–nucleon (YN) interaction by the Nijmegen [1–3] group and Bonn–Jülich [4,5] group. In these models, the short-range forces have been treated with phenomenological methods. On the other hand, the quark-cluster model (QCM) approaches, which describe the short-range forces based on quark and gluon dynamics, have been developed independently by the groups from Tokyo [6,7], Tübingen [8] and Kyoto–Niigata [9].

The parameters of these models were determined by fitting the existing experimental data of the NN and YN scattering. However, as for the YN scattering, there are only very limited data. Due to the short lifetime of the hyperons, a device which can observe complicated reaction topologies in the region of approximately a cm about the reaction vertex is needed to perform a YN scattering experiment in the low-momentum region (below 1 GeV/c). In this region, almost all experiments were performed with bubble chambers in the 1960's [10–17]. Since the bubble chambers required the low beam rates, the stopping K^- method was the most efficient way to produce hyperons. As for Σp scattering, because most experiments [10–12,16] used this method, the momenta of the Σ's were limited to be less than 200 MeV/c. In this region, S-waves are expected to be dominant. For example, in Ref. [16], the allowed region for the Σ^+p scattering lengths was determined by applying the effective range approximation assuming S-wave predominance. All models used only these low-momentum Σp scattering data to

determine their parameters. They have not been tested with experimental data at higher momenta, where the contributions from the P- and higher partial waves are important. It should be noted that important information of the NN interaction, such as the spin-dependent forces and hard core, was provided from NN scattering experiments up to 800 MeV/c. Experimental studies of YN scattering in momentum regions higher than previous experiments (up to 1 GeV/c) are urgently needed.

As a first step of these efforts, a Σ^+p scattering experiment was performed at KEK-PS (E251) [18]. The experiment E251 was aimed at measuring the differential cross section of the Σ^+p scattering with a new technique using a scintillating fiber (SCIFI) active target. The SCIFI detector system had a better time resolution (~ 2 μs) than that of bubble chambers. It enabled us to use the 5×10^4/s π^+ beam and to record only the relevant pictures event by event. With the SCIFI detector, the in-flight reactions could be used to measure the Σ^+p scattering at higher momentum, which was not possible with bubble chambers. Σ^+'s of 300 to 700 MeV/c were produced through the in-flight $p(\pi^+, \mathrm{K}^+)\Sigma^+$ reaction with a 1.6 GeV/c pion beam. Only the (π^+, K^+) events were recorded by using an external trigger system. A plastic scintillating fiber block, which was developed for the H-dibaryon search [19], was used as a production target for hyperons, a Σ^+p scattering target, and a 4π detector for the related charged particles around the reaction vertices. The reaction topologies were recorded as digitized image data. As a next step, we performed experiment E289 to measure the Σ^-p and Λp scattering cross sections, and to obtain more statistics on the Σ^+p scattering data. It is important to measure all channels in order to check the assumption of flavor $SU(3)$ symmetry in the YN interaction models. We measured the three reaction channels with the same setup. The SCIFI target system was improved regarding several points. The effective volume was larger than that of the previous one to observe Λ's whose lifetime is longer than that of Σ's. Also, thinner scintillating fibers were adopted to improve the spatial resolution.

In this paper, we present the result of the measurement of the differential cross sections for Σ^-p elastic scattering. The momentum region is from 400 to 700 MeV/c where no differential cross section data exist. In this region, contributions from P-waves and higher partial-waves appear in the elastic cross sections. The momentum dependence is also presented.

2. Experiment

The experiment was carried out at the K2 beam line of the 12 GeV Proton Synchrotron (PS) at KEK. Fig. 1 shows a top view of the experimental setup. A 1.32 GeV/c π^- beam was used to produce Σ^-'s through the (π^-, K^+) reaction. Outgoing K^+'s were identified with a K^+ spectrometer system. A scintillating fiber (SCIFI) target was used as the production and scattering target. It also worked as a 4π tracking detector for the charged particles and as a range counter for the charged particles stopped in the SCIFI block. We could identify the hyperons, which may be scattered and decay inside the SCIFI target.

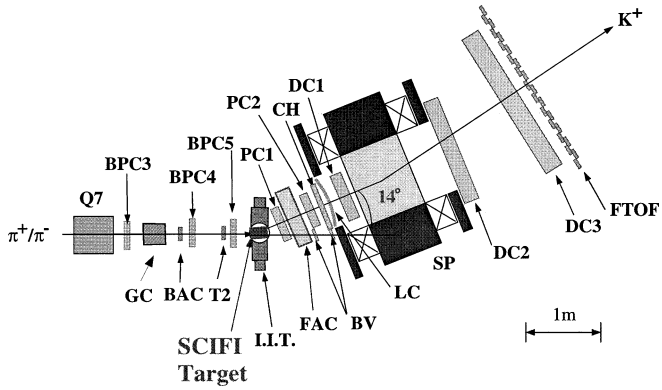

Fig. 1. Schematic view of the experimental setup.

2.1. The π^- beam

The typical intensity of the separated π^- beam was 1.5×10^5 /spill ($\sim$ 2 s). The momentum was 1.32 GeV/c with a spread of $\Delta p/p = 0.7\%$ (r.m.s.). The contamination of electrons and μ^-'s was 13% and that of $\bar{\mathrm{p}}$'s and K^-'s was less than 1%. The e^-'s and μ^-'s were vetoed with a gas Čerenkov counter (GC), and the $\bar{\mathrm{p}}$'s and K^-'s were eliminated with an aerogel Čerenkov counter (BAC). The contamination was reduced to be less than 0.1%. The tracking of the beam particles was performed with multiwire proportional chambers (BPC3-5). To check the online trigger and to confirm the particle identification, the time-of-flight was measured with scintillation counters (T1,T2), where T1 was located 7 m upstream of the SCIFI target. The TOF resolution (T2–T1) was $\Delta t = 55$ ps (r.m.s.).

2.2. The K^+ spectrometer

On-line and off-line particle identification (P.I.D.) of outgoing particles from the SCIFI target were performed with the K^+ spectrometer system. In order to avoid any overlapping of the K^+ and Σ^- tracks in the SCIFI pictures, the acceptance of the spectrometer did not cover 0 degree in the horizontal direction; it covered from 4 to 24 degrees. The pion background was rejected with the forward aerogel Čerenkov counter (FAC). The momentum of an outgoing particle was approximately calculated with the combination of a hodoscope (CH) located just before a dipole magnet (SP) and a TOF array (FTOF) at the most downstream end of the spectrometer. This momentum information and the PID information obtained from the Čerenkov counters were used for the first-level trigger. In addition, by using the momentum information and the TOF information obtained from the FTOF and T2, the mass of an outgoing particle was selected with a set of fast-encoding electronics (Lecroy FERA–FERET system) to reduce the proton background at the second-level trigger (Mass Trigger). The decision times of the first- and second-level triggers were 360 ns and within 15 μs, respectively. The typical trigger rate was $5 \sim 8$ /spill. The momentum of an outgoing particle was calculated with use of the SP, MWPC's (PC1-2) and drift chambers (DC1-3) in the off-line analysis. The integrated magnetic field along the

tracks of outgoing particles in the SP was 0.94 T m in average. The momentum resolution was $(\Delta p/p) = 1.0\%$ (r.m.s.) at $p = 0.7$ GeV/c. To reconstruct the mass of an outgoing particle, the velocity of the particle was also obtained by measuring the TOF between T2 and FTOF. The TOF resolution (FTOF–T2) was $\Delta t = 140$ ps (r.m.s.) in the off-line analysis.

2.3. The SCIFI active target system

The SCIFI block consisted of 300 μm × 300 μm square plastic scintillating fibers (KURARAY SCSF-78 [20]). The core material of the fiber was polystyrene ($(CH)_n$) and the size was 288 μm × 288 μm. The refractive index of the core was 1.59 and the density was 1.05 g/cm^3. The cladding was made of polymethylmethacrelate (PMMA, $C_5H_8O_2$) with refractive index of 1.49 and density of 1.19 g/cm^3. The attenuation length was measured to be 114 cm with a ^{90}Sr β-ray source. The wavelength of the transmitted light was peaked at 450 nm. The SCIFI block was assembled by stacking fiber sheets alternately, as shown in Fig. 2. Each fiber sheet consisted of about 330 fibers, which corresponded to 100 mm in width. The fiber sheets were bonded with white paint, which eliminated any cross talk over the fiber sheets by diffused reflection of the untrapped photons. About 600 sheets were used to create an effective volume of 100 mm × 100 mm × 200 mm. The fiber sheets of each direction were bundled at the readout arms to make readout surfaces of 100 mm × 100 mm. At the other ends of the fibers, aluminum evaporated lucite-plates were attached as mirrors, which improved the effective attenuation length by a factor of three.

The output light from the SCIFI was amplified with two sets of image-intensifier (II) chains. Fig. 3 shows a schematic structure of the II chain. The II chain consisted of four II's. The first (HAMAMATSU V4440PX [21]) and second (DEP PP0030X [22]) stages were electrostatic-type II's. The diameters of the input and output windows of the first II were 100 mm ∅ and 25 mm ∅, respectively. The quantum efficiency of the photo-cathode was about 20%. In order to hold the images until the trigger would be fired, phosphors were used at the output window of each II, except for the fourth stage. The phosphor of the first II was PS-5, with a decay-time of which was 1.3 μs. This decay-time limited the

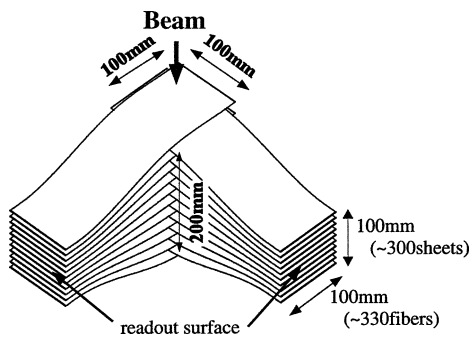

Fig. 2. Schematic view of the structure of the SCIFI block.

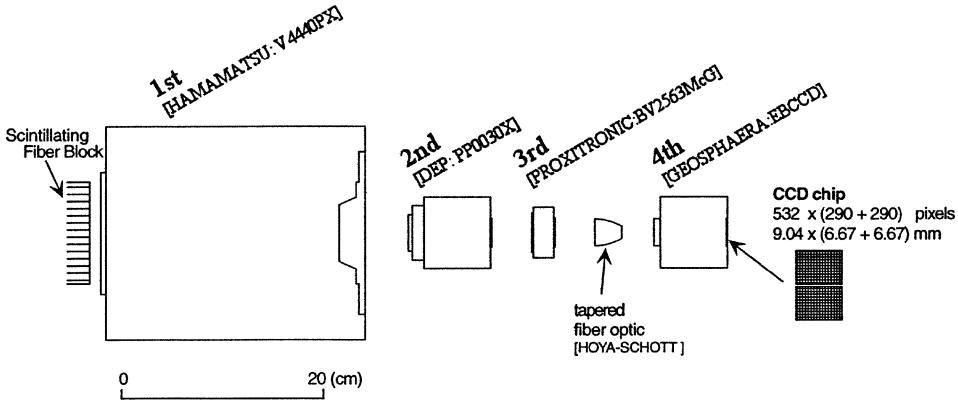

Fig. 3. Schematic structure of the image intensifier (II) chain.

acceptable beam rate for the SCIFI target to less than a few $\times 10^5$/spill. The diameters of both the input and output windows of the second II were 25 mm ∅. The P46 phosphor with a decay-time of 300 ns was used for the second II. The first and second II's were operated in DC mode. The operating voltages for the first and second II were 20 kV and 15 kV, and the photon gains were both ~ 10.

The third stage (PROXITRONIC BV2563McG [23]) was a micro-channel–plate (MCP) type. The diameters of the input and output windows were 25 mm ∅, and the decay-time of the phosphor (P20) for the third II was 20 μs. The gain of the third II was $\sim 10^3$.

At the fourth stage, an electron bombarded CCD system (GEOSPHAERA EBCCD [24]) was used. The third II and EBCCD were gated by the first-level and second-level triggers, respectively. The output window of the third II and the input window of the EBCCD were connected through a tapered fiber-optic. On the input window of the EBCCD, the size of the image was reduced to 8 mm in diameter, which fitted the effective size of the CCD chip. The intensified photon images were read out by the EBCCD and recorded as digitized image data. The photo-electrons were accelerated and bombarded the back side of the CCD chip, and the EBCCD itself had a gain of 10^3. The CCD chip consisted of 532 × 580 pixels, where the size of one pixel was 17 μm × 23 μm. The effective area on the CCD chip was 9.04 mm × 13.34 mm. The frame transfer to read out the charge on the CCD was started by the external trigger. The driving clock rate of the CCD was 10 MHz and the readout time was 45 ms. The images were digitized with a 6-bit ADC. Fig. 4 shows an example of image data.

The performance of the SCIFI system was investigated with the 1.32 GeV/c minimum-ionizing π^-'s and slow Σ^-'s whose typical momenta were about 500 MeV/c. For the 1.32 GeV/c π^- tracks, photons from the fibers are recognized as the cluster of active pixels. The average number of hit fibers (hit density) along the track was 0.25 /sheet, and the residual of the cluster around the fitted line was 165 μm. This value is consistent with the calculated one determined with the size of the fiber and CCD pixel, the distortion of the II and the error of position calibration. For the track of the Σ^-, the clusters were stuck together and it was difficult to recognize each cluster, since the energy deposit of

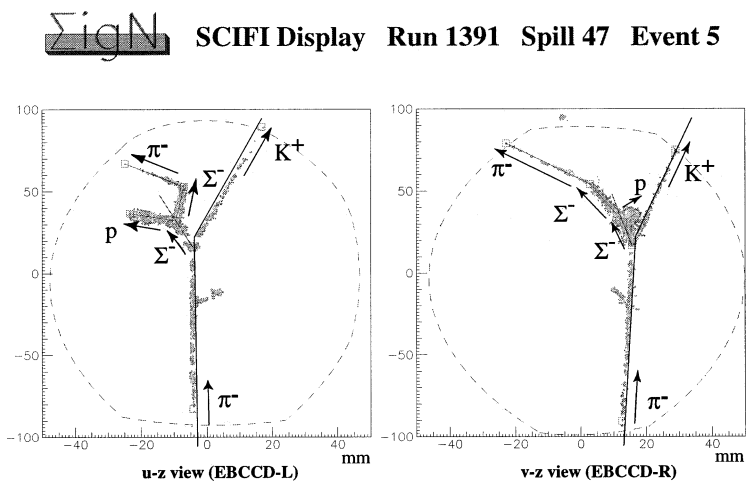

Fig. 4. An example of a Σ^-p scattering event observed with the SCIFI detector. The open squares represent the input positions from the pointing process and the solid lines on the incoming π^- and outgoing K^+ are the results of the tracking with the external wire chambers. The lines from the (π^-, K^+) vertices correspond to the predicted momentum vectors of the initial Σ^- (see text).

the 500 MeV/c Σ^- is about four-times larger than that of the 1.32 GeV/c π^-. The track width is, therefore, defined as the distribution of each active pixel around the track, and the track width of the Σ^- track was 440 μm (r.m.s.).

3. Analysis

3.1. Identification of the (π^-, K^+) reaction

The number of collected events was 4.3×10^6. The (π^-, K^+) events were selected by reconstructing the mass of the outgoing particles with the K^+ spectrometer. Fig. 5 shows the mass spectrum of the outgoing particles. The particles whose reconstructed mass were within 0.4 to 0.6 GeV/c^2 were regarded as K^+'s. The K^+ mass resolution was $\Delta M =$ 15 MeV/c^2 (r.m.s.) at a momentum of 0.7 GeV/c, and the background contamination was estimated to be less than 1.3%. The vertex of the (π^-, K^+) reaction was obtained by tracking the incoming and outgoing particles with wire chambers, and the vertex was required to be in the region of $-100 < z < 100$ mm, where the direction of the z-axis was along the π^- beam-line and the origin was the center of the SCIFI target. The tracking efficiency was 91%.

3.2. Event categorization and pointing

The pictures of the selected (π^-, K^+) events were eye-scanned manually and categorized according to their image patterns on the video pictures. The number of scanned events was 2.8×10^5. About 65% of these events were Σ^- production events:

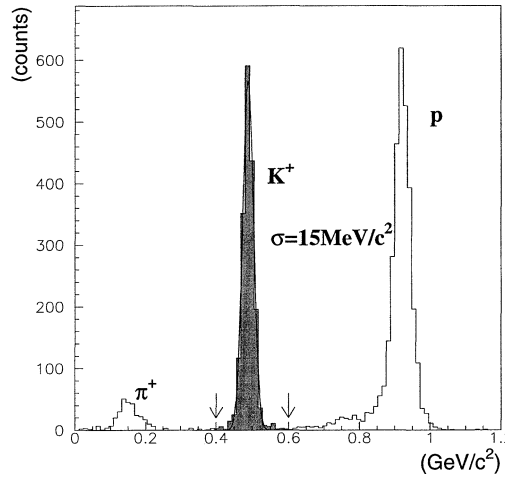

Fig. 5. Mass spectrum of the outgoing particles. The hatched area was recognized as K^+'s.

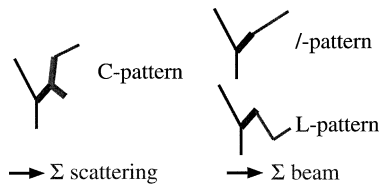

Fig. 6. Patterns for the event categorization. The event topology was recognized as a combination of these patterns.

$$\pi^- + \mathrm{p} \rightarrow \mathrm{K}^+ + \Sigma^-. \tag{1}$$

The scanned events included other reactions, for example,

$$\pi^- + \mathrm{p} \rightarrow \mathrm{K}^+ + \Sigma^{*-}, \qquad \Sigma^{*-} \rightarrow \Lambda + \pi^-, \tag{2}$$

which are not discussed in this paper. Some of the Σ^-'s reacted with protons:

$$\Sigma^- + \mathrm{p} \rightarrow \Sigma^- + \mathrm{p}, \tag{3}$$

$$\Sigma^- + \mathrm{p} \rightarrow \Sigma^0 + \mathrm{n}, \tag{4}$$

$$\Sigma^- + \mathrm{p} \rightarrow \Lambda + \mathrm{n}. \tag{5}$$

In this paper, only the elastic scattering (3) is discussed.

The event topology was recognized as a combination of patterns. For example, the weak decay of the $\Lambda \rightarrow \mathrm{p}\pi^-$ was recognized as a 'V-pattern', and the decay of the Σ was recognized as a '/-pattern'. The event patterns which were necessary to derive the cross section of the $\Sigma^-\mathrm{p}$ elastic scattering are shown in Fig. 6. The (π^-, K^+) vertex was obviously recognized with the help of the guide lines on the event display obtained from the wire chambers. If a track of an emitted particle from the (π^-, K^+) vertex kinked only once, this track was recognized as the '/-pattern'. Even if the track was straight, a change in the brightness of the track was regarded as a kink. In case there were more than two

kinks, the track was recognized as the 'L-pattern'. The events including the '/-pattern' or 'L-pattern' are Σ^- beam candidates. The first kink of the '/-pattern' and 'L-pattern' corresponds to the decay of the Σ^-, and the following kinks correspond to the decay or scattering of the π^- which is a decay product of the Σ^-; the branching ratio of $\Sigma^- \to \pi^-$n is 100%. As for the 'L-pattern', the first kink may be a Σ^- scattering without a visible recoil proton, but such a event is easily recognized by the brightness of the tracks, and was not used for the analysis. The number of such events was negligible compared to the events regarded as the Σ^- beam. The 'C-pattern' consists of one straight track (prong) and one kinked track. The events including the 'C-pattern' are candidates for the Σ^-p scattering. For the identification of the Σ^-p elastic scattering event, one visible recoil proton track was required, and the prong in the 'C-pattern' corresponds to this proton. The kink corresponds to the decay of the scattered Σ^-. The number of the Σ^- beam candidates was 1.8×10^5 and the number of the Σ^-p scattering candidates was 776.

After event categorization was completed, the reaction points were marked on a graphic display with a pointing device. The reaction points were determined 3-dimensionally by these marks. We call this process 'pointing'. The pointing was done for 2947 samples of the Σ^- beam candidates and all events of the Σ^-p scattering candidates.

The efficiencies of the eye-scanning and all other analyzing processes described below were estimated by a set of Monte Carlo simulations. Simulated image data were generated by the same method as described in Ref. [18], and the parameters to reproduce the picture were tuned for the conditions of the present experimental apparatus. The generated image data were analyzed through the same process as the real data, and the efficiencies were evaluated from the surviving rates of the simulation events. The angular resolution and the accuracy of the track-length measurements were also estimated using the simulation data by comparing the generated positions to the positions obtained by the pointing process. For short tracks, the accuracies of the angle and length measurements and the scanning efficiencies decrease, as shown in Fig. 7. Therefore, for the events including short tracks, the event identification is ambiguous, and especially, the angular resolution becomes not sufficient to distinguish the background, which is mainly from quasi-free scattering, as described later. In order to avoid these ambiguities, a set of geometric criteria was required for further analysis. For both the Σ^- beam and Σ^-p scattering candidates, track-length of the Σ^- was required to be more than 5 mm, and for Σ^-p scattering candidates, the track-lengths of the scattered Σ^- and the recoil proton were required to be more than 3 mm. The production vertex of the (π^-, K^+) reaction was reconstructed more precisely by using the image data in addition to the wire chambers. The vertex resolution along the z-axis was estimated to be 0.6 mm from the simulation data. To avoid ambiguities in the categorization for events which occurred at the upstream and downstream ends of the SCIFI, the z-position of the vertex was required to be within $-90 \sim 60$ mm. The recoil protons for Σ^-p scattering candidates were required to stop inside at least one of the fiducial areas of $u-z$ and $v-z$ views, where the definition of $u-z$ and $v-z$ views is shown in Fig. 4. The fiducial area was defined to be inside of the ellipse whose long axis was 180 mm in the beam direction and short axis was 90 mm, which correspond to the input

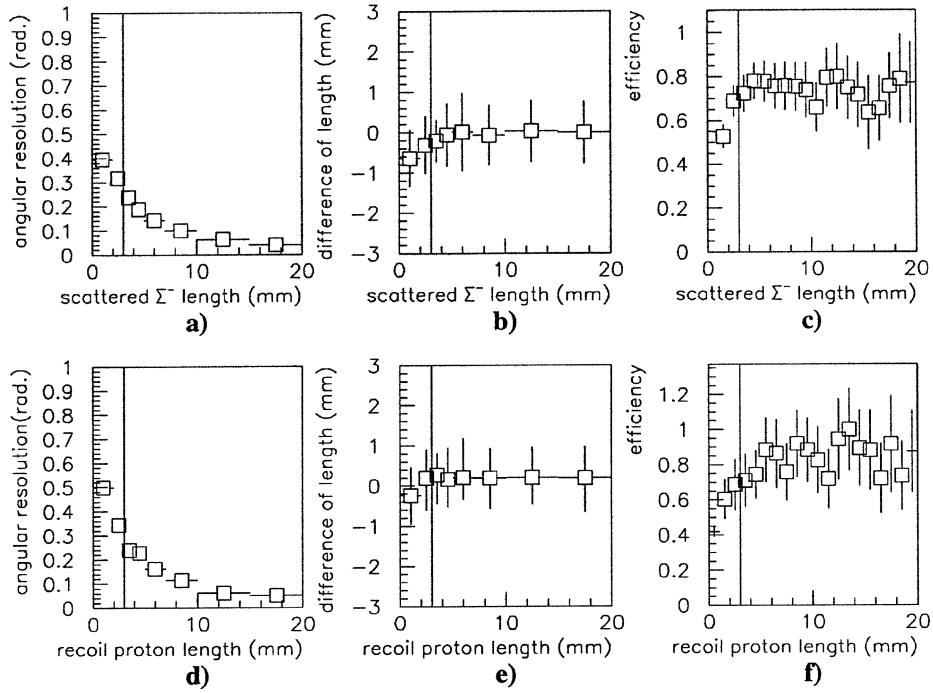

Fig. 7. Track-length dependence for the scattered Σ^- track of the (a) angular resolution (r.m.s.), (b) deviation of the track length and (c) efficiency of the pointing process; (d), (e) and (f) are for the recoil proton track. They were obtained from the analysis of the simulated image data. The lines represent the threshold of the track-length cut.

window of the first II. The stopping point of the recoil proton was also required to be inside the effective volume of the SCIFI target.

3.3. Total flight length of the Σ^-'s

The Σ^-'s are produced through both the reaction on free protons and the quasi-free process on carbon nuclei, since the SCIFI target consists of $(CH)_n$. Only the Σ^-'s produced on free protons were used as the Σ^- beam, because the momenta of the Σ^-'s from carbon nuclei are ambiguous due to the Fermi motion. The selection was done by applying angle-difference and missing-mass cuts. The angle-difference for the Σ^- production kinematics ($\Delta\theta_{\mathrm{prod}}$) was defined as

$$\Delta\theta_{\mathrm{prod}} = \cos^{-1}\left(\frac{\vec{p}_{\Sigma^-\mathrm{prod}} \cdot \vec{v}_{\Sigma^-\mathrm{prod}}}{|\vec{p}_{\Sigma^-\mathrm{prod}}||\vec{v}_{\Sigma^-\mathrm{prod}}|}\right), \tag{6}$$

where $\vec{v}_{\Sigma^-\mathrm{prod}}$ is the measured direction of the Σ^- obtained from the pointing process, and $\vec{p}_{\Sigma^-\mathrm{prod}}$ denotes the predicted momentum vector of the Σ^- calculated from the momentum vectors of the π^- and the K^+. The momenta of the π^- and K^+ were obtained from the analysis of the spectrometer data, and the directions were measured with the SCIFI detector and external wire chambers.

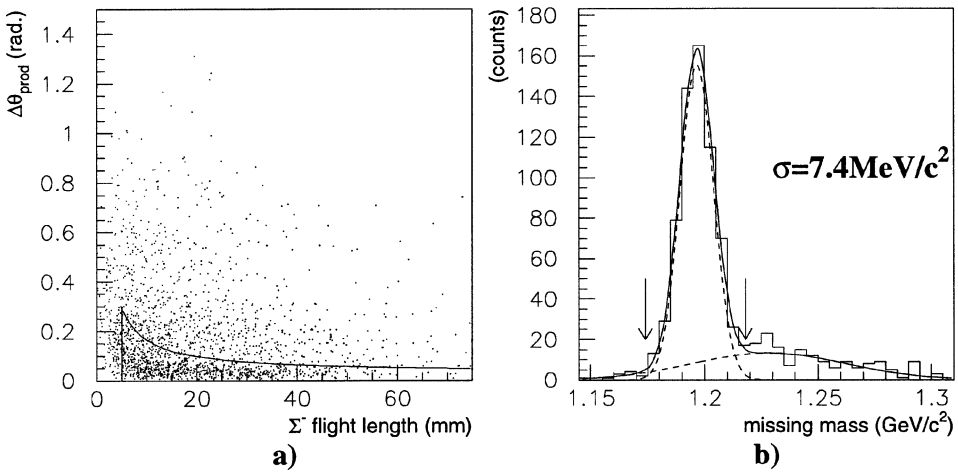

Fig. 8. (a) Scatter plot of $\Delta\theta_{\rm prod}$ versus the flight length of the Σ^- (ℓ_{Σ^-}). (b) Missing-mass spectrum of the $p(\pi^-, \mathrm{K}^+)X$ reaction after the angle-difference cut was applied. The lines on the spectrum are obtained with a two-Gaussian fitting. The events inside the region indicated by the arrows were regarded as the Σ^- produced on the free proton.

Fig. 8(a) shows the distribution of $\Delta\theta_{\rm prod}$ versus the flight length of the Σ^- (ℓ_{Σ^-}). The $\Delta\theta_{\rm prod}$ distributes around zero within the resolution of the SCIFI system for the Σ^-'s produced on the free protons. These events make a narrow peak, and which can be distinguished from the broader distribution of the quasi-free events. The region inside the lines in Fig. 8(a) was the accepted region for the Σ^-'s produced on the free protons. The threshold was set to be

$$\Delta\theta_{\rm prod} < \frac{1.35}{\ell_{\Sigma^-}} + 0.03, \qquad \ell_{\Sigma^-} > 5\ \mathrm{mm}, \tag{7}$$

by taking projections of Fig. 8(a) onto $\Delta\theta_{\rm prod}$ in some slices of ℓ_{Σ^-}. Fig. 8(b) shows the missing-mass spectrum of the $p(\pi^-, \mathrm{K}^+)X$ reaction after the angle-difference cut was applied. The missing-mass resolution was 7.4 MeV/c^2 (r.m.s.). The events whose missing-mass were calculated to be from 1.174 to 1.218 GeV/c^2 were regarded as the Σ^-'s produced on free protons. The contamination from the quasi-free process was estimated to be 10%.

The amount of the Σ^- beam was defined as the total flight length of the Σ^-'s (FL_{Σ^-}), where $FL_{\Sigma^-} = \sum(\ell_{\Sigma^-} - \ell_{\rm th})$. Here, ℓ_{Σ^-} is the flight length for each event and the $\ell_{\rm th}$ is the threshold length, which was set to be 5 mm, as shown in Section 3.2. Using with the 2947 pointed data sample, the total flight length of the Σ^-'s produced on free protons was measured to be 963 ± 33 cm. The efficiency for this length measurement was estimated with the simulation event being 0.827 ± 0.026. Taking into account this efficiency, for all of the Σ^- beam candidates, the number of which was 1.8×10^5, FL_{Σ^-} of the Σ^-'s produced on free protons was estimated to be $(7.13 \pm 0.33) \times 10^4$ cm.

3.4. $\Sigma^- p$ scattering events

The number of Σ^-p scattering candidates which satisfied the criteria described in Section 3.2 was 311. Because the Σ^-'s were required to be produced on free protons, the same cuts as described in Section 3.3 were applied, reducing the number of events to 88. Additionally, cuts on the angle-difference and missing-mass were also applied to the scattering kinematics to eliminate the background, which was mainly from quasifree scattering on the carbon nuclei. The angle-difference for the scattering kinematics ($\Delta\theta_{\mathrm{scat}}$) was defined as

$$\Delta\theta_{\mathrm{scat}} = \cos^{-1}\left(\frac{\vec{p}_{\Sigma^-\mathrm{scat}} \cdot \vec{v}_{\Sigma^-\mathrm{scat}}}{|\vec{p}_{\Sigma^-\mathrm{scat}}||\vec{v}_{\Sigma^-\mathrm{scat}}|}\right). \tag{8}$$

Here, $\vec{v}_{\Sigma^-\mathrm{scat}}$ is the measured direction of the scattered Σ^- by the pointing, and $\vec{p}_{\Sigma^-\mathrm{scat}}$ denotes the predicted momentum vector of the scattered Σ^- calculated from the momenta of the initial Σ^- and recoil proton. The momentum of the initial Σ^- was determined from the kinematics of the (π^-, K^+) reaction, taking the energy loss in the SCIFI target into account. The momentum of the initial Σ^- just before scattering ranged from 400 MeV/c to 700 MeV/c and the momentum resolution was 13 MeV/c (r.m.s.). The momentum of the recoil proton was calculated from the range in the SCIFI.

Fig. 9(a) shows the distribution of $\Delta\theta_{\mathrm{scat}}$ versus the flight length of the scattered Σ^-, and the region surrounded by the lines is the accepted region for elastic events. The accepted region was parameterized as

$$\Delta\theta_{\mathrm{scat}} < \frac{1.0}{fl_{\Sigma^-\mathrm{scat}}} + 0.06, \quad fl_{\Sigma^-\mathrm{scat}} > 3\ \mathrm{mm}. \tag{9}$$

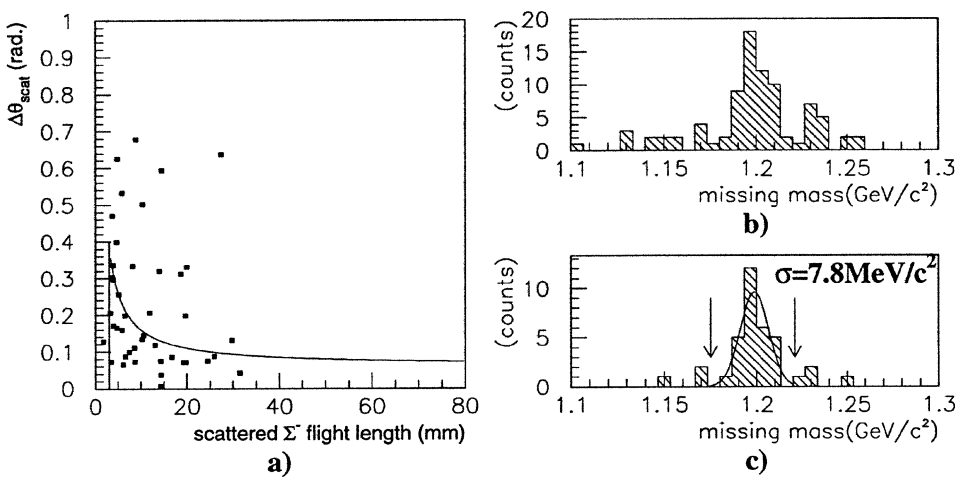

Fig. 9. (a) Distribution of the angle-difference $\Delta\theta_{\mathrm{scat}}$ versus the flight length of the scattered Σ^-'s. The definition of $\Delta\theta$ is described in the text. The region inside the lines is the accepted region. (b) Missing-mass spectrum of the Σ^-p scattering before the angle-difference cut was applied. (c) After the angle-difference cut was applied. The missing-mass resolution was 7.8 MeV/c^2. The region between the arrows was accepted as Σ^-p elastic scattering.

This threshold was determined with the same distribution as in Fig. 9(a) obtained from the simulation data of the Σ^-p elastic scattering, because the statistics for real data was not sufficient. Fig. 9(b) shows the missing-mass spectrum of the $p(\Sigma^-, \mathrm{p})X$ reaction before the angle-difference cut was applied and Fig. 9(c) is the one after the cut was applied. The events whose missing-mass were $1.175 \sim 1.221\ \mathrm{GeV}/c^2$ were recognized as elastic events. An example of a picture of an elastic scattering event is shown in Fig. 4. Finally, 30 events survived after all of the cuts were applied. The scattering angle in the center of mass (CM) system (θ_{CM}) was calculated with the momenta and directions of the initial Σ^- and recoil proton. The accuracy of the scattering angle was $\Delta(\cos\theta_{\mathrm{CM}}) = 0.09$ (r.m.s.).

The amount of background contamination was estimated using the simulation data. The simulation events of the quasi-free scattering were generated and were normalized to reproduce the tail of the $\Delta\theta_{\mathrm{scat}}$ distribution of the real data, as shown in Fig. 10. The same cuts as for real elastic events were applied and the survived events were regarded as the contamination from quasifree events. The error of the normalization was ±25%. This caused a systematic error of ±40% for the cross section in the region $-0.5 < \cos\theta_{\mathrm{CM}} < -0.2$; for other angular regions, however, these errors were estimated to be less than ±3%. In addition, there was the contamination from the quasifree Σ^- production. For the Σ^-p scattering events, this contamination was 7%, and the systematic error for the cross section was 3%, because the Σ^- beam events also included this contamination of 10%. The total analyzing efficiency was obtained from the analysis of the simulated data of the Σ^-p elastic scattering. The yields, estimated backgrounds and efficiencies for each angular region are summarized in Table 1. The errors of the track-length measurement cause an uncertainty on the efficiency. The systematic deviation of the track-length was estimated to be less than 0.3 mm with the simulated image data. The effect of this uncertainty on the cross section was estimated to be ±7% by generating a systematic deviation of ±0.3 mm

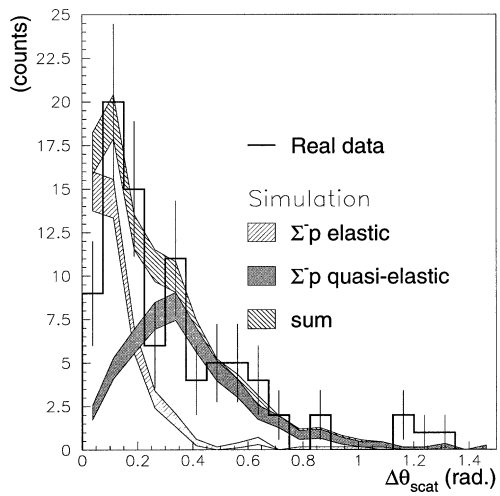

Fig. 10. Distribution of $\Delta\theta_{\mathrm{scat}}$ obtained from the real data and the simulation data of the elastic and quasi-elastic Σ^-p scattering. The hatched band represents the simulation data.

Table 1
The yields of the Σ^-p elastic events, estimated backgrounds, total efficiencies, and differential cross sections. Except the cross sections, only the statistical errors were displayed. The errors for no. of events correspond to a probability of 68.3% for a Poisson distribution

$\cos\theta_{\rm CM}$	Number of events	Background	Background subtracted	Efficiency	$\frac{d\sigma}{d\Omega}$ ± stat. ± sys. (mb/sr)
$-0.5--0.2$	$1^{+2.3}_{-0.8}$	0.62 ± 0.22	$0.4^{+2.3}_{-0.9}$	0.20 ± 0.04	$0.3^{+1.8}_{-0.7} \pm 0.1$
$-0.2-0.1$	$9^{+4.1}_{-2.9}$	0.69 ± 0.23	$8.3^{+4.1}_{-3.0}$	0.43 ± 0.06	$3.0^{+1.5}_{-1.1} \pm 0.3$
$0.1-0.4$	$11^{+4.4}_{-3.3}$	0.62 ± 0.22	$10.4^{+4.4}_{-3.3}$	0.47 ± 0.06	$3.4^{+1.5}_{-1.1} \pm 0.3$
$0.4-0.7$	$9^{+4.1}_{-2.9}$	0.85 ± 0.26	$8.2^{+4.1}_{-3.0}$	0.34 ± 0.05	$3.7^{+1.9}_{-1.4} \pm 0.3$

in the analysis of the simulation data. In the derivation of the cross section, the target was assumed to be made of $(CH)_n$, and the materials of the cladding and white paint were neglected. If these materials are taken into account, the effect on the cross section is about 2%. The systematic errors of the cross sections given in Table 1 include all of those listed above.

4. Result and discussions

The differential cross sections were derived from

$$\frac{d\sigma}{d\Omega} = \frac{N_{\rm scat}}{FL_{\Sigma^-} \cdot \rho_t \cdot d\Omega}. \tag{10}$$

Here, $N_{\rm scat}$ is the number of scattering events corrected by the efficiency factor. The FL_{Σ^-} is the total flight length of the Σ^- beam obtained in Section 3.3, and ρ_t represents the number density of the protons in the SCIFI target, which is $4.87\times10^{22}/{\rm cm}^3$.

The experimental results are summarized in Table 1. The statistical errors include the errors on the real data and the errors from the statistics of the simulated image data. The systematic error for $-0.5 < \cos\theta_{\rm CM} < -0.2$ is dominated by the error from the background subtraction, and the errors for other angular regions are from the errors on length measurements, as described in Section 3.4. In this channel, since the difference between the models is not so large, we compare our results to typical two calculations. Fig. 11 shows a plot of the differential cross sections together with theoretical calculations from the OBE model [25] and QCM [26]. The momenta of the Σ^-'s for the calculations are 0.5 GeV/c. The error bars represent only statistical ones. In Fig. 11, Jülich means the OBE model of the Bonn–Jülich group (model A in [4,5]). The Bonn–Jülich model is based on the spin–flavor $SU(6)$ symmetry and contains 2π-exchange, replacing the scalar meson exchange. Form factors, which were parameterized by the cutoff mass Λ_α, are used at each vertex. The FSS is one of the QCM calculations of the Kyoto–Niigata group [9]. They are using the resonating group method (RGM) with antisymmetrized six-quark wave functions. In both models, the forward-peaking structures appear, which are

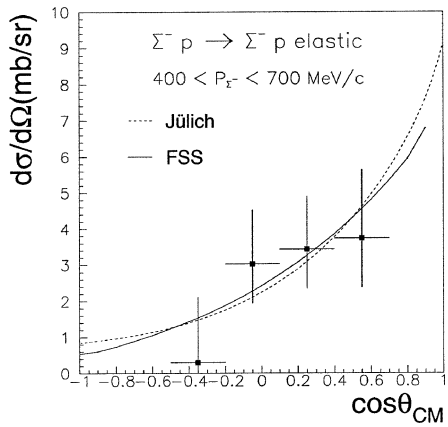

Fig. 11. Differential cross section for Σ^-p elastic scattering. The dashed line represents the theoretical calculation by the Bonn–Jülich group with their OBE model (model A), and the solid line is by the Kyoto–Niigata group with their quark-cluster model (FSS).

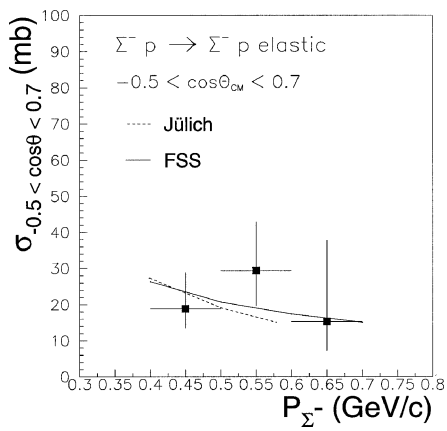

Fig. 12. Integrated cross section for Σ^-p elastic scattering. The solid line represents the theoretical calculation with FSS and the dashed line is the Bonn–Jülich model A. (This model can be used in the region less than about 0.58 GeV/c, i.e. below the threshold for pion production.)

the contributions of P-waves. Both models are in reasonably good agreement with our experimental data.

The momentum dependence of the experimental data is shown in Fig. 12. The plotted values are the integrated cross sections in the angular region of $-0.5 < \cos\theta < 0.7$, they are 19^{+10}_{-5} mb ($0.4 < p_{\Sigma^-} < 0.5$ GeV/c), 29^{+14}_{-10} mb ($0.5 < p_{\Sigma^-} < 0.6$ GeV/c), and 15^{+23}_{-8} mb ($0.6 < p_{\Sigma^-} < 0.7$ GeV/c). The errors are statistical ones. The momentum dependence of the data is consistent with the FSS and the Bonn–Jülich model A within the statistical errors.

5. Summary

We have presented the results of a measurement of the differential cross sections for Σ^-p elastic scattering in the momentum region from 400 to 700 MeV/c where no differential cross section data existed. We have also measured the differential cross section for Σ^+p and Λp scattering, and these results will be presented in separate papers.

The experiment was carried out at the K2 beam line of KEK 12 GeV PS. A 1.32 GeV/c π^- beam was used to produce the Σ^-'s via the (π^-, K^+) reaction, and the scattering and decay of Σ^- were observed with a scintillating fiber (SCIFI) active target system. The SCIFI target consisted of about 200000 scintillating fibers, and image data were read out with image intensifiers (II's) as digitized image data. The 2.8×10^5 pictures were eye-scanned, and 776 Σ^-p scattering candidates and 2947 samples of Σ^- beam candidates were analyzed. To select the Σ^-p elastic scattering events, geometrical and kinematic cuts were applied; 30 events survived as Σ^-p scattering events.

The Σ^-p elastic scattering differential cross sections have been compared with the Bonn–Jülich model A and the quark-cluster model calculation of the Kyoto–Niigata group (FSS). The present result is in good agreement with both theoretical calculations. The momentum dependence is also consistent with the theoretical calculations.

Acknowledgements

We wish to thank staffs of the KEK PS for their support during the experiment and analysis. We thank Professors H. Sugawara, S. Yamada, K. Nakamura, Y. Yoshimura, and J. Chiba for their continuous encouragement throughout this work. We would like to thank Prof. J. Haidenbauer, who provided the theoretical calculation of Bonn–Jülich model. We express our appreciation to Prof. Y. Fujiwara and Dr. T. Fujita for their theoretical calculation of Kyoto–Niigata model. This work was supported partially by Grants-in Aid for Scientific Research No. 06640425 of Japan Ministry of the Education, Science and Culture. Some of authors (H.K and Y.K) were supported by JSPS Research Fellowships for Young Scientists.

References

[1] M.M. Nagels, T.A. Rijken, J.J. de Swart, Phys. Rev. D 15 (1977) 2547; Phys. Rev. D 20 (1979) 1633.
[2] P.M.M. Maessen, T.A. Rijken, J.J. de Swart, Phys. Rev. C 40 (1989) 2226.
[3] T.A. Rijken, V.G. Stokes, Y. Yamamoto, Phys. Rev. C 59 (1999) 21.
[4] B. Holzenkamp, K. Holinde, J. Speth, Nucl. Phys. A 500 (1989) 485.
[5] A. Reuber, K. Holinde, J. Speth, Nucl. Phys. A 570 (1994) 543.
[6] M. Oka, K. Yazaki, in: W. Weise (Ed.), Quarks and Nuclei, World Scientific, 1984, p. 489.
[7] K. Yazaki, in: T. Yamazaki, K. Nakai, K. Nagamine (Eds.), Perspectives of Meson Science, Elsevier, 1992, p. 795.
[8] U. Straub, Z.Y. Zhang, K. Bräuer, A. Faessler, S.B. Khadkikar, G. Lübeck, Nucl. Phys. A 483 (1988) 686; Nucl. Phys. A 508 (1990) 385c.

[9] Y. Fujiwara, C. Nakamoto, Y. Suzuki, Prog. Theor. Phys. 94 (1995) 215; Prog. Theor. Phys. 94 (1995) 353; Phys. Rev. Lett. 76 (1996) 2242; Phys. Rev. C 54 (1996) 2180.
[10] H.G. Dosch et al., Phys. Lett. 21 (1966) 236.
[11] R. Engelmann et al., Phys. Lett. 21 (1966) 587.
[12] H.A. Rubin et al., Phys. Rev. 159 (1967) 1149.
[13] B. Sechi-Zorn et al., Phys. Rev. 175 (1968) 1735.
[14] G. Alexander et al., Phys. Rev. 173 (1968) 1452.
[15] G.R. Charlton et al., Phys. Lett. B 32 (1970) 720.
[16] F. Eisele et al., Phys. Lett. B 37 (1971) 204.
[17] J.A. Kadyk et al., Nucl. Phys. B 27 (1971) 13.
[18] J.K. Ahn et al., Nucl. Phys. A 648 (1999) 263.
[19] J.K. Ahn et al., Phys. Lett. B 378 (1996) 53.
[20] KURARAY Co. Ltd., Maruzen Building, 3-10, 2-Chome, Nihonbashi, Chuo-ku, Tokyo 103-0027, Japan.
[21] HAMAMATSU Photonics, 314-5, Shimokanzo, Toyooka-village, Iwata-gun, Shizuoka, 438-0193, Japan.
[22] Delft Electronishe Producten (DEP), NL-9300 AB Roden, The Netherlands.
[23] PROXITRONIC, Robert-Bosch-Strasse 34, D 64625 Bensheim, Germany.
[24] GEOSPHAERA, Case Postale No. 6, Moscow, 117133, Russia.
[25] J. Haidenbauer, private communications.
[26] Y. Fujiwara and T. Fujita, private communications.